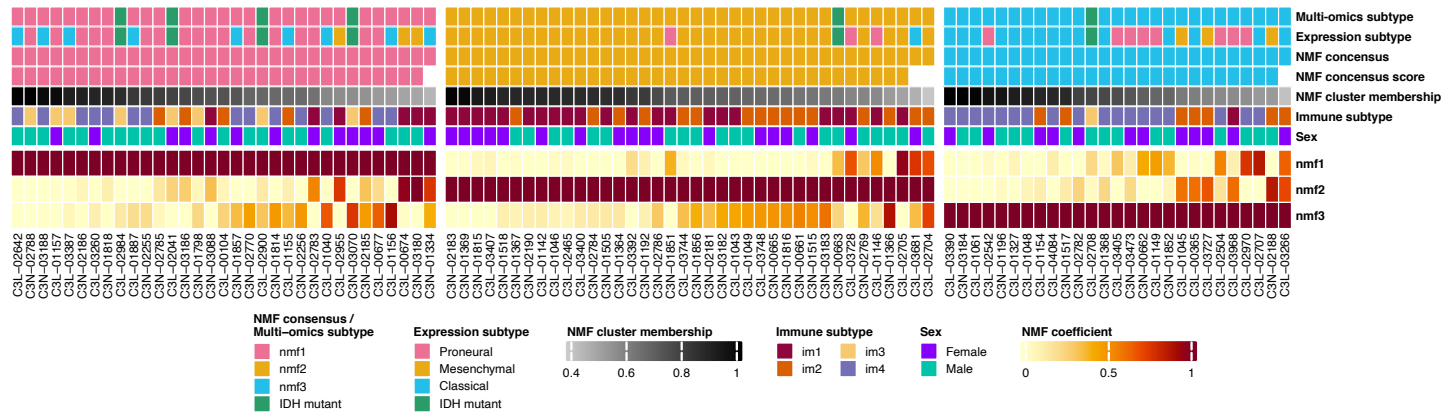
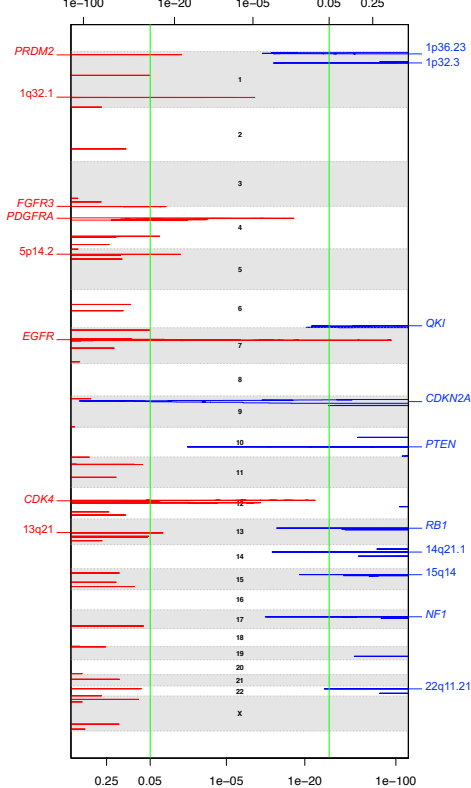
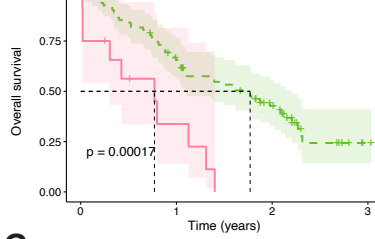
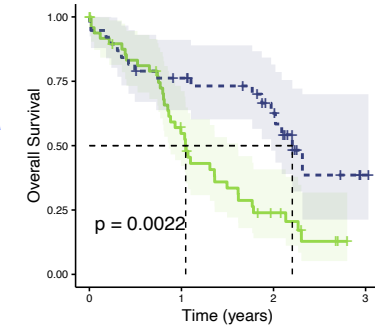
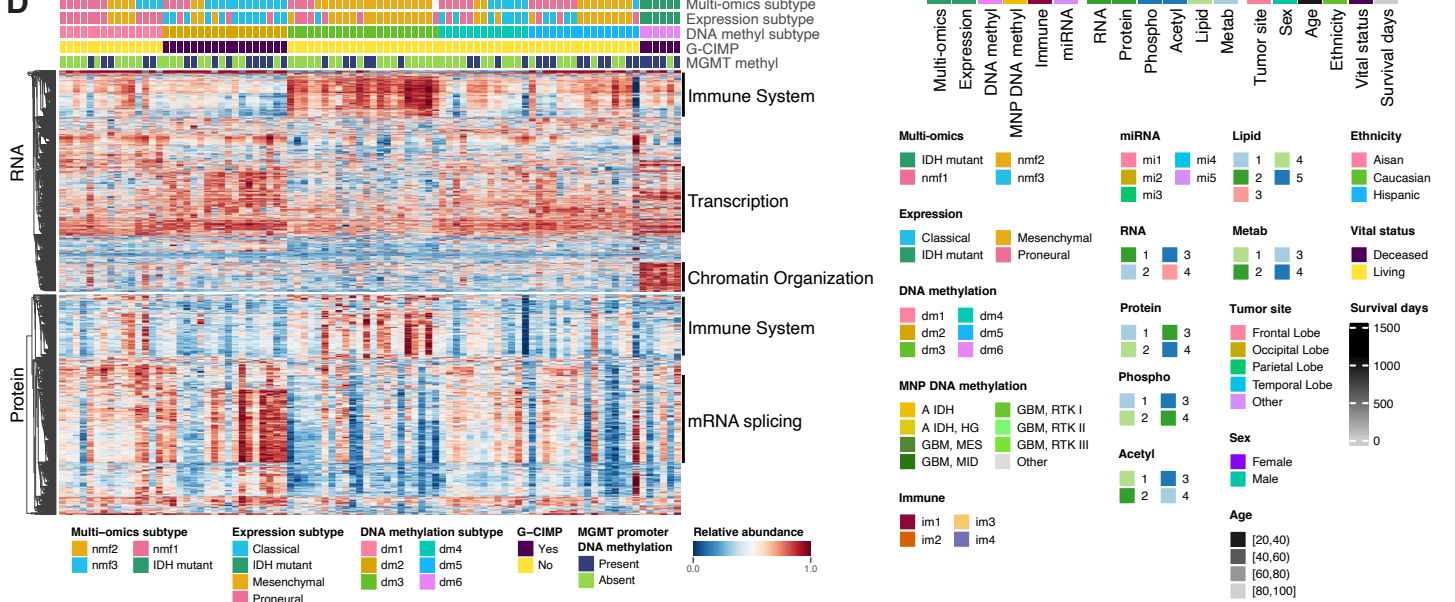
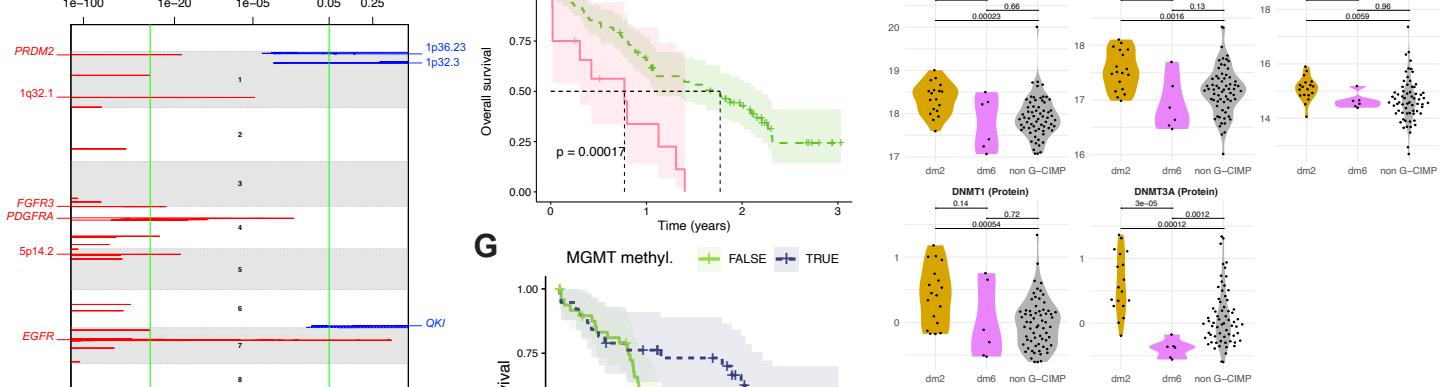
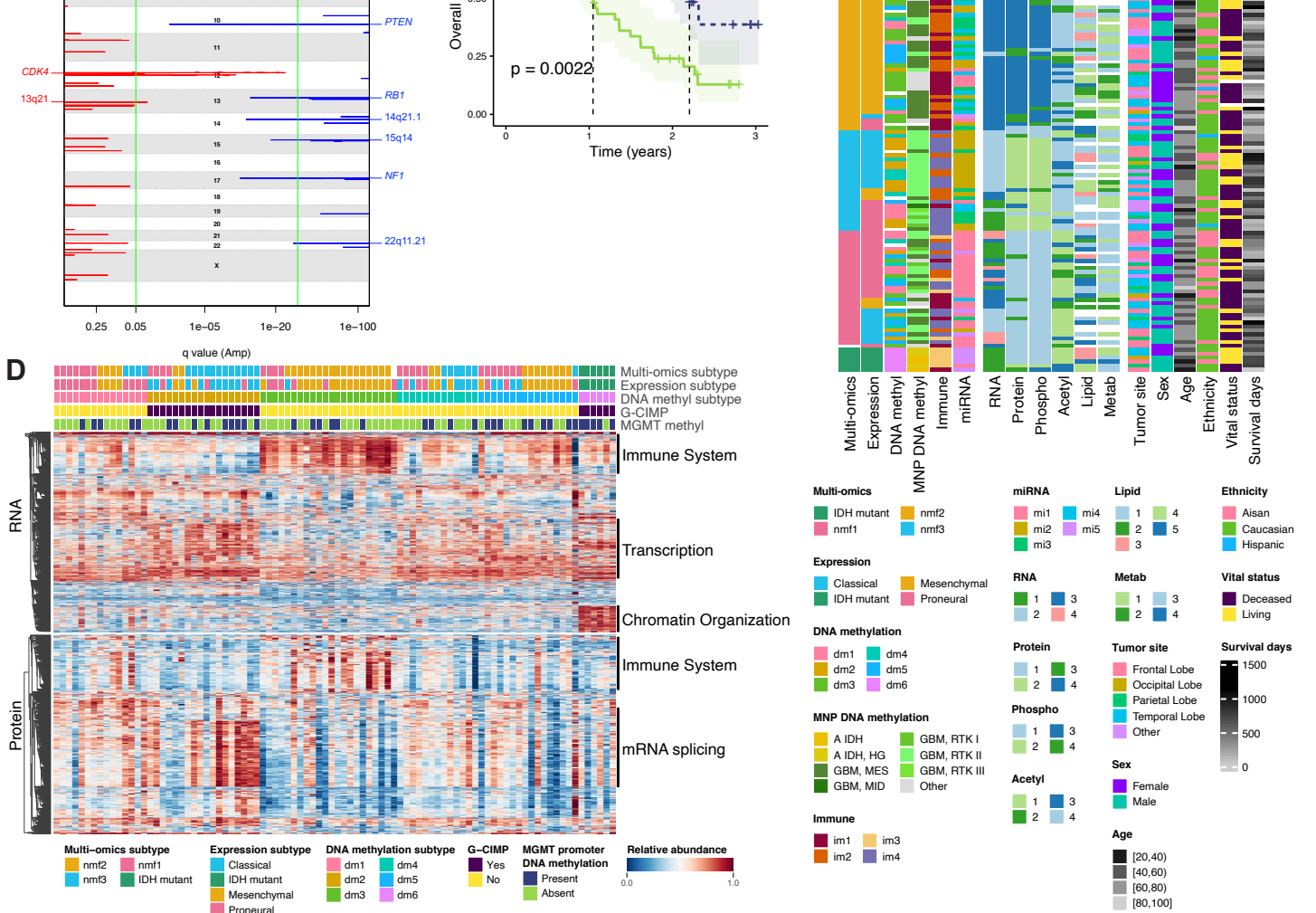


## **Figure S1. Integrated Proteomic Workflow and Quality Control, Related to Figure 1.**

A) TMT-11 based global proteome, phosphoproteome, and acetylome analysis workflow. The GBM tumors and GTEx normal tissues were analyzed in 11 TMT 11-plex experiments, each with 10 study samples and a common internal reference sample created by pooling all study samples (equal contribution). The TMT11-labeled samples were then fractionated, split (with 5% peptide mass analyzed directly for global proteome), and subjected to tandem enrichment of phosphopeptides and acetylated peptides. Peptides were detected and quantified using information from the TMT-11 MS/MS spectra.

B) Distribution of sequence coverage of the identified proteins with tryptic peptides detected by MS/MS in each TMT-11 plex; whiskers show the 5–95 percentiles. The total numbers of identified proteins in each TMT plex range from 9,992 to 10,572.

C) Robust and precise proteomics platforms. Longitudinal performance was tested by repeated proteome, phosphoproteome and acetylome analysis of aliquots of the same patient-derived xenograft QC samples in standalone TMT-11 plexes, along with the GBM study samples; scatter plots and Pearson correlations comparing individual replicate measurements are shown.

**B****A****C****G****D****E****F**

**Figure S2. Proteogenomic Characterization and Subtyping of GBM, Related to Figure 1.**

- A) GISTIC2 copy number variations at and focal level of all tumors with WGS available.
- B) Heatmap of multi-omics membership scores of all three multi-omics subtypes for each tumor.
- C) Survival Kaplan–Meier curves of mixed-subtype tumors with low multi-omics membership score versus the rest of the tumors.
- D) Pathway enrichment analysis of gene expression with differential DNA methylation in promoter regions across all six DNA methylation subtypes.
- E) Differentially expressed DNMTs in two G-CIMP subtypes (dm2 and dm6) at both RNA and protein level.
- F) Comparison of the clustering results using individual data type, including DNA methylation, miRNAs, RNAs, proteins, phosphoproteins, acetylproteins, lipids, and metabolites.
- G) Survival Kaplan–Meier curves of tumors with different MGMT promoter DNA methylation status.

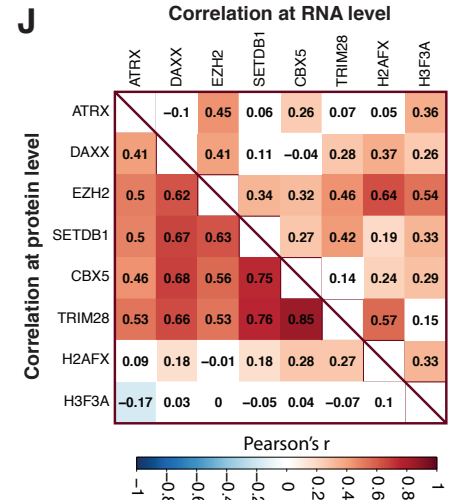
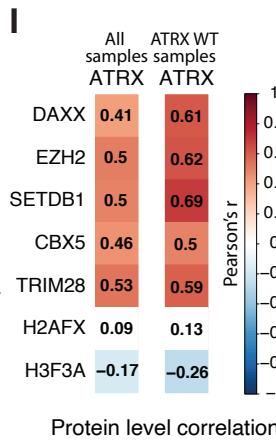
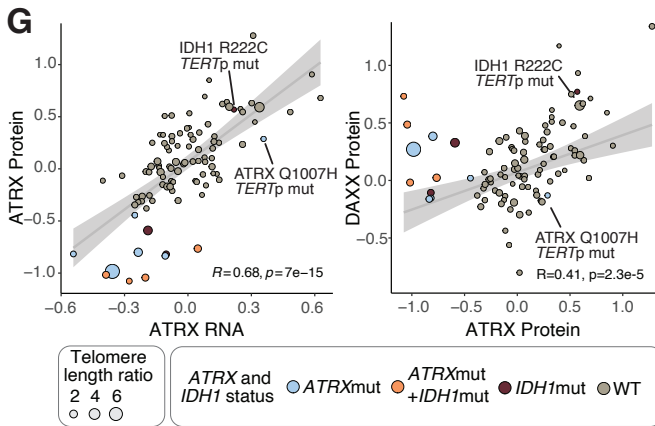
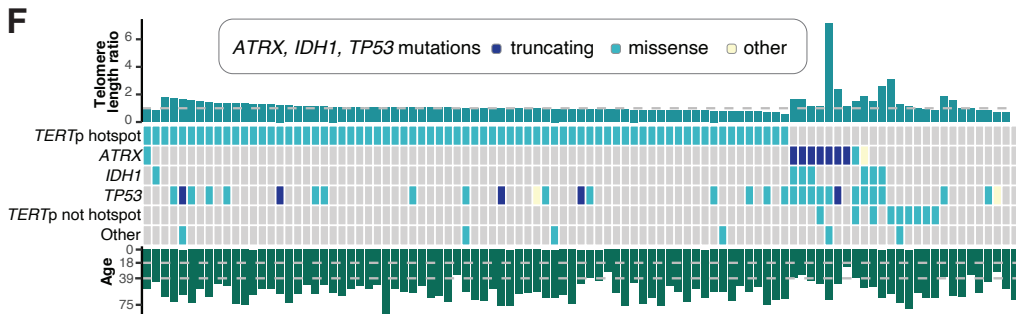
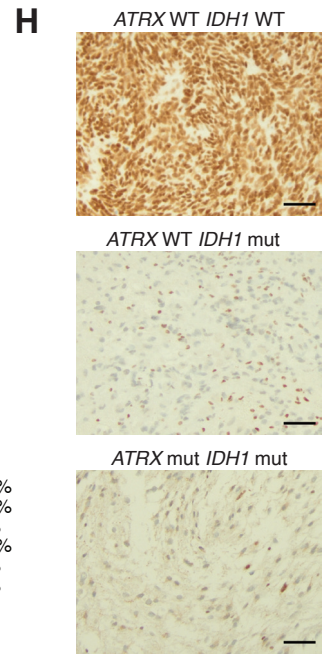
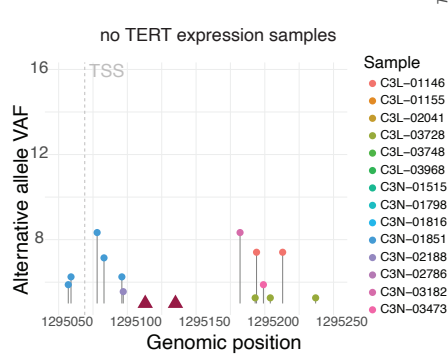
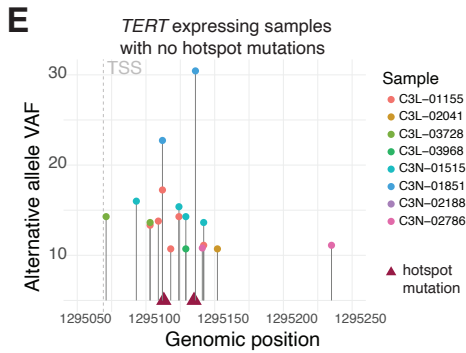
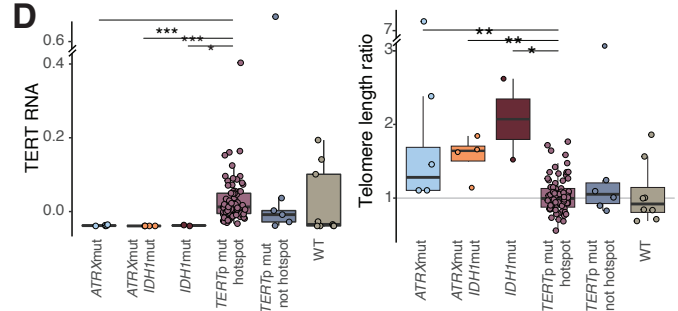
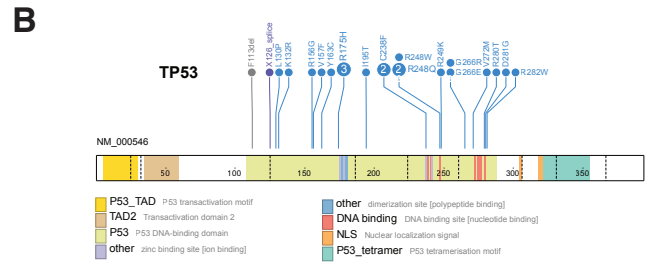
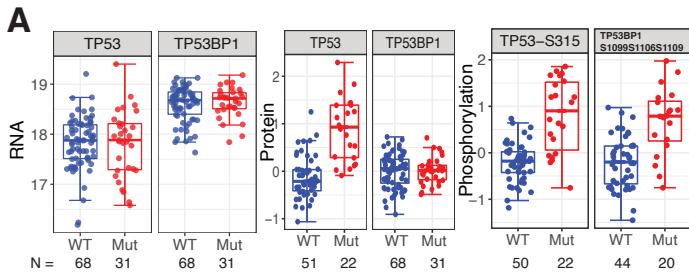


### Figure S3. Effect of *TP53*, *TERTp*, *IDH1*, and *ATRX* Mutations, Related to Figure 2.

- A) Boxplots showing RNA, protein and phosphosite abundance for *TP53* and *TP53BP1* in *TP53*-WT tumors (blue; n=68) and *TP53*-mutated tumors (red; n=31).
- B) The lollipop of *TP53* mutations in **Figure 2C**.
- C) IGV screenshot of RNA supporting reads for alternative splice site associated with *TP53* X126\_ splice mutation.
- D) *TERT* RNA expression in proposed telomere genotypes. *TERTp* mutations are associated with stable *TERT* expression (left). Telomere length ratio (WGS tumor telomere length / WGS blood normal telomere length) in proposed telomere genotypes (right).
- E) Variant allele frequency of mutations in *TERTp* region found in tumors not carrying *TERTp* hotspot mutations but expressing *TERT* RNA (upper panel) and in tumors not carrying *TERTp* hotspot mutations and no expressing *TERT* RNA (bottom panel). For the upper panel mutations with > 10% VAF are shown, for the bottom panel mutations with > 5% VAF are shown. Triangles indicate hotspot genomic position 1295113 and 1295135 (-124 and -146 bp from TSS labeled by the dashed line).
- F) Overview of genetic alterations in *TERTp* hotspot and not hotspot positions, mutations in *ATRX*, *IDH1* and *TP53*. Telomere length ratio in tumor/blood normal is indicated on top, patient age is indicated in the bottom.
- G) *ATRX* and *IDH1* mutational effect on *ATRX* RNA and protein levels. *IDH1* R132H mutations affect *ATRX* protein only (left). Neither *ATRX* nor *IDH1* mutations are associated with reduced DAXX protein expression (right). The missense *ATRX* mutant, Q1007H, residing outside of the SNF2 and helicase domains, had normal RNA and protein expression. We noticed that other gene mutations also led to altered *ATRX* protein levels, including significantly decreased *ATRX* protein in *IDH1* R132H mutants, even though the *ATRX* RNA level itself appeared unchanged
- H) Immunohistochemistry staining for *ATRX* protein in FFPE sections of *ATRX* WT and *IDH1* WT tumor (positive), *ATRX* WT and *IDH1*mut tumor (negative), and in *ATRX*mut and *IDH1*mut tumor (negative). IHC staining confirmed low *ATRX* expression in *IDH1* mutants regardless of *ATRX* mutational status. Scale bars: 100  $\mu$ m.
- I) WT *ATRX* protein is better correlated with its complex partners than if WT and mutant combined together.
- J) *ATRX* complex members showed high correlation of their abundance in protein but not in RNA across all tumors.



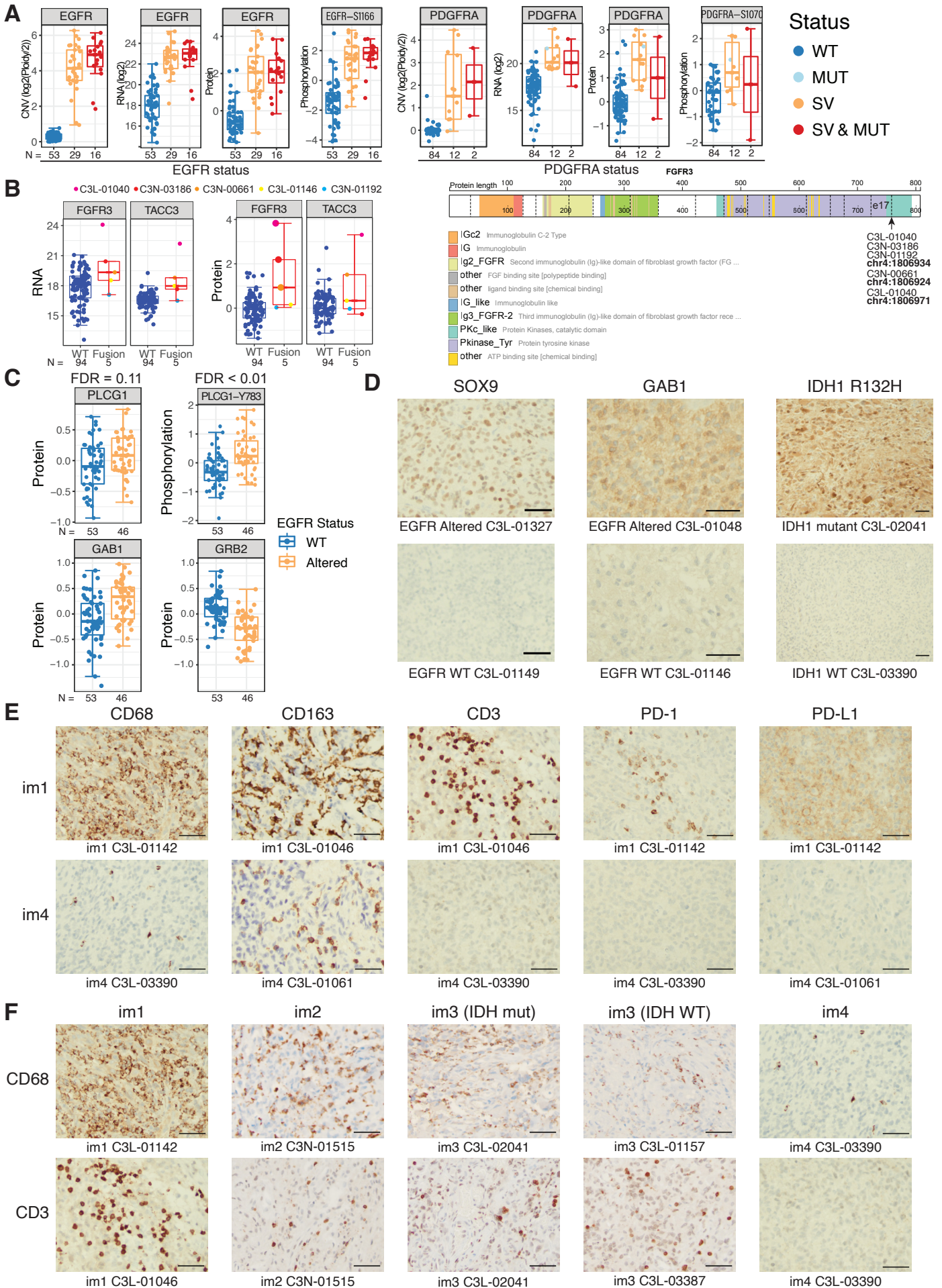


**Figure S4. CNV, RNA, Protein and Phosphosite Level Change in Samples with Different RTK Alterations, and Immunohistochemistry Staining Results, Related to Figures 2, 3 and 4.**

A) The comparison of CNV, RNA and protein expressions and phosphosite level between *EGFR* altered and WT samples (left panel) and *PDGFRA* altered and WT samples (right panel). We did not find expression differences between samples having a sole SV event versus those with dual mutation and SV events, suggesting *EGFR* upregulation in GBM is largely due to SV, as associated with CNV amplification, rather than mutationally driven, which is different from other tumor types, such as lung cancer (Cancer Genome Atlas Research Network, 2014). We also found nine samples in which *EGFR* SV co-occurred with *PDGFRA* or *FGFR3* SV, while 13 samples with either *PDGFRA* or *FGFR3* alteration did not show any alterations in *EGFR*. For *PDGFRA*, two out of three mutations overlap with SV events. Only one sample with mutation in *PDGFRA* had high *PDGFRA* RNA and protein expression. For *EGFR*, n=53 (WT), 29 (SV), and 16 (SV and MUT); for *PDGFRA*, n=84 (WT), 12 (SV), and 2 (SV and MUT).

B) The comparison of RNA and protein expression of *FGFR3* and *TACC3* between samples with and without *FGFR3-TACC3* fusion and the breakpoints found in *FGFR3* from RNA-Seq data (n=94 and 5, respectively). Five samples with *FGFR3-TACC3* fusions with an intact *FGFR3* kinase domain. Three samples which are protein expression outliers in *FGFR3* are marked by larger circles.

C) The comparison of *PLCG1*, *GAB1*, and *GRB2* protein expression and *PLCG1-Y783* phosphosite level between *EGFR* altered (n=53) and WT (n=46) samples.

D) Immunohistochemistry staining for *SOX9* and *GAB1* expression in *EGFR* altered and WT tumors is concordant with the mass spectrometry findings. Positive *IDH1* R132H staining of the *ATRX* WT and *IDH1* mutant tumor shown in **Figure 2H**. Scale bars: 100  $\mu$ m.

E) Immunohistochemistry staining for *CD68*, *CD163*, *CD3*, *PD-1*, *PD-L1* in tumors of different immune subtypes is concordant with the mass spectrometry and gene expression analyses. Scale bars: 100  $\mu$ m.

F) Immunohistochemistry staining for *CD68* and *CD3* in tumors of all four immune subtypes is concordant with the mass spectrometry and gene expression analyses. Scale bars: 100  $\mu$ m.



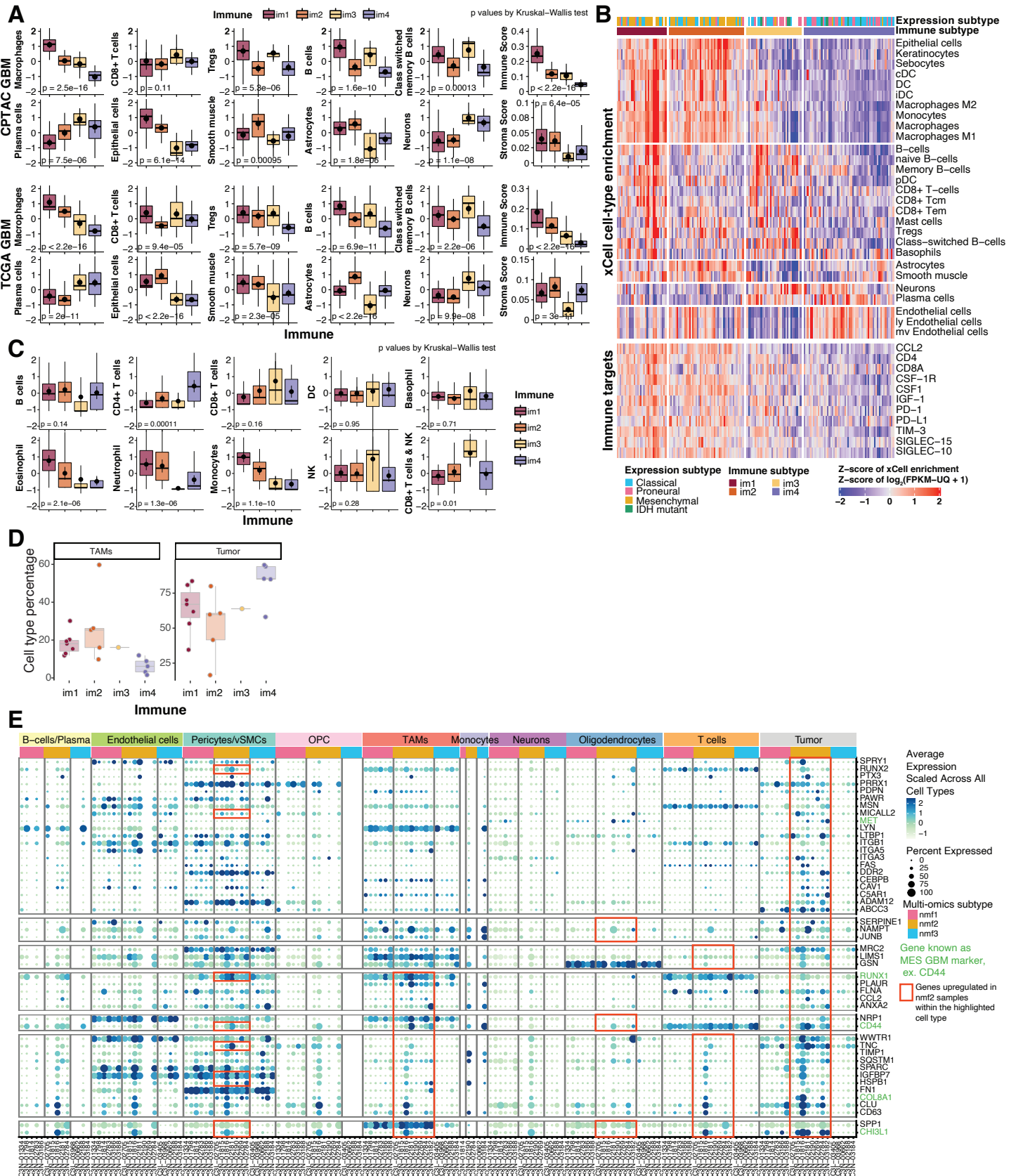


**Figure S5. Distinct Immune Marker Expression Ascertains Immune Subtypes, Related to Figure 4.**

- A) The distributions of xCell cell type enrichments, immune scores, and stroma scores among the 4 immune subtypes in the CPTAC GBM cohort and TCGA GBM cohort. For CPTAC, n=30 (im1), 28 (im2), 9 (im3), and 32 (im4); for TCGA, n=32 (im1), 48 (im2), 35 (im3), and 59 (im4).
- B) The 4 immune subtypes identified by the consensus clustering on the cell type enrichment in the TCGA GBM study.
- C) The distributions of protein-based CIBERSORT cell type enrichments among the 4 immune subtypes in the CPTAC GBM cohort. N=30 (im1), 28 (im2), 9 (im3), and 32 (im4).
- D) snRNA-seq cell type percentage per sample in each immune subtypes.
- E) Expression of epithelial–mesenchymal transition genes from different cell types in different snRNA-seq samples. Genes upregulated (Wilcoxon FDR < 0.05 and  $\log_2FC > 0.25$ ) in tumor cells of nmf2 samples. Genes were also tested for significant upregulation in TAMs, T-cells, oligodendrocytes and pericytes/vSMCs; the same thresholds were applied to genes highlighted in red boxes. Dot size denotes the percentage of cells expressing a gene in the given cell type.

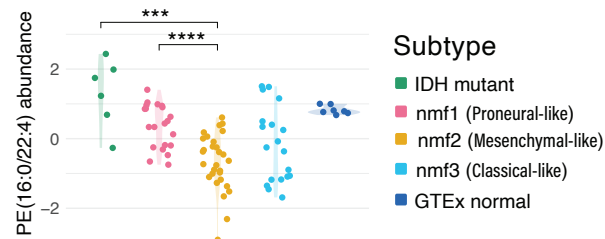
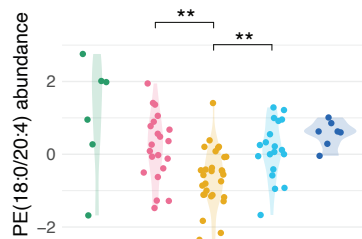
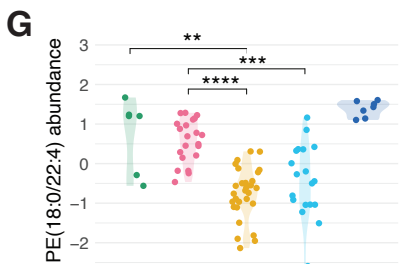
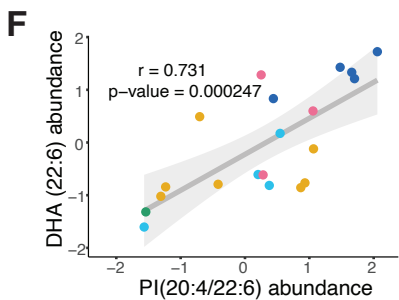
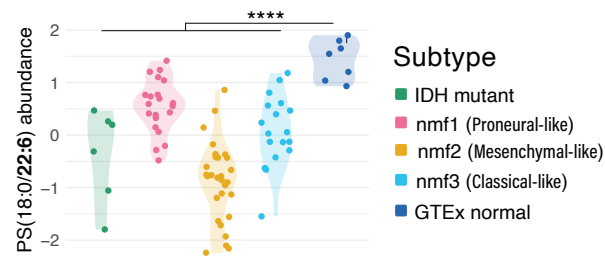
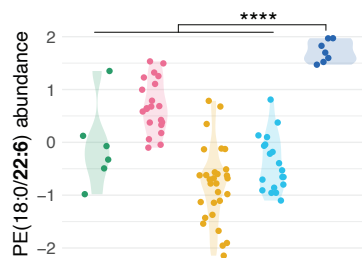
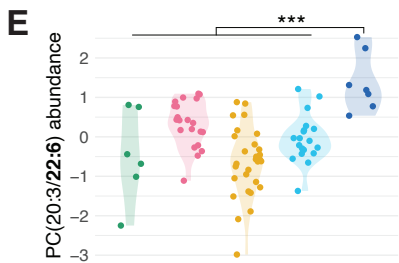
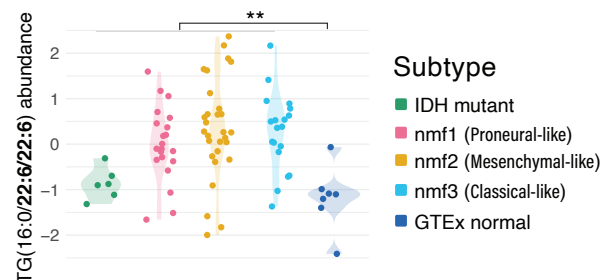
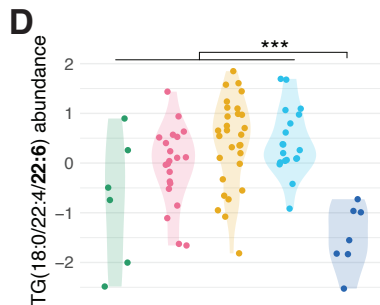
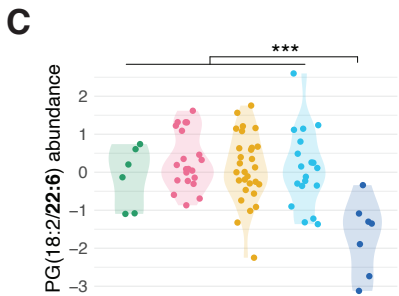
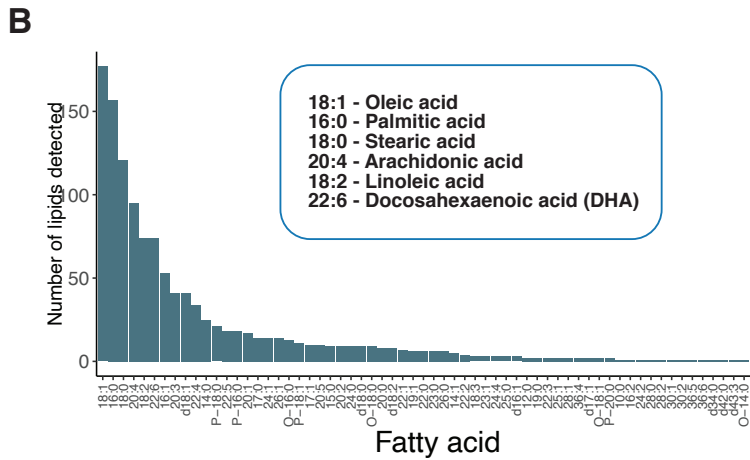
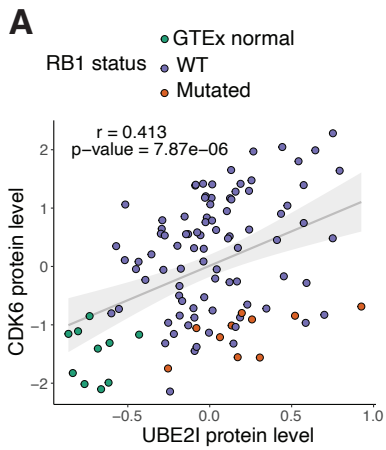
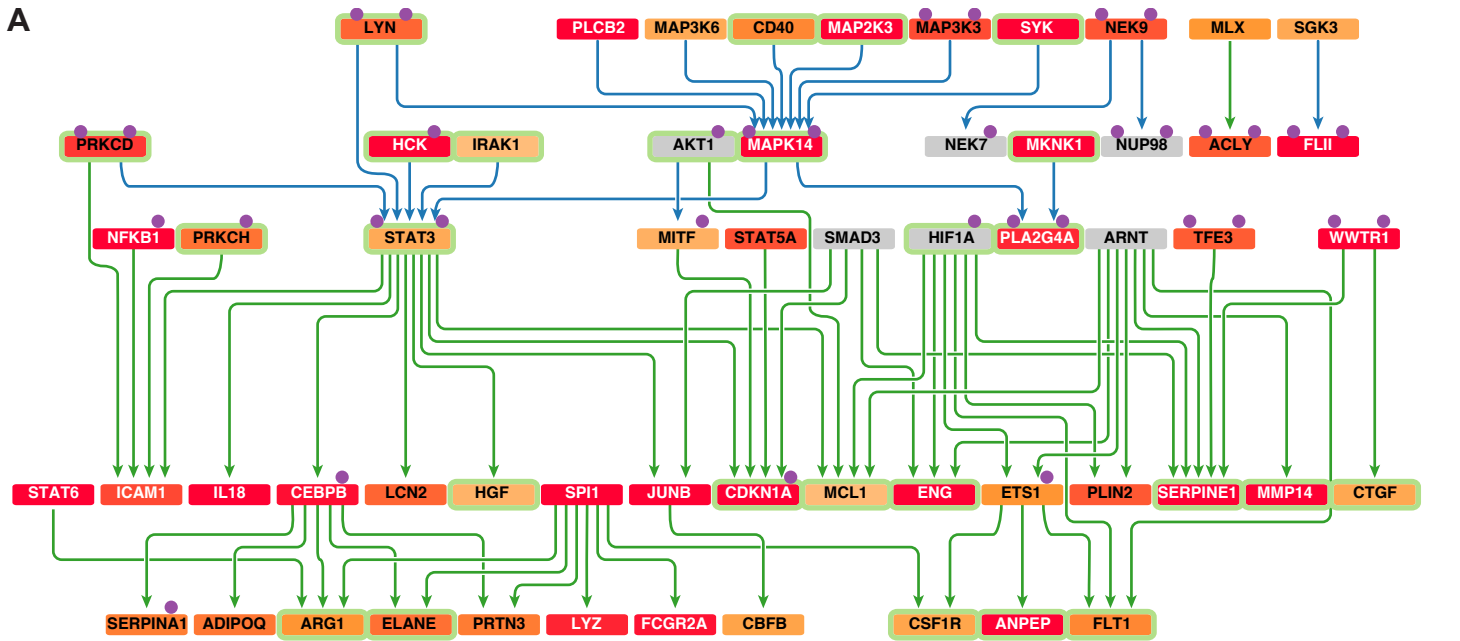


**Figure S6. Relations Between H2B Acetylation and SUMOylation Pathway, Related to Figure 5; Additional Lipid Abundance Evidence, Related to Figure 6.**

- A) Scatterplot showing correlation between UBE2I protein level and CDK6 protein level. Pearson's correlation value and  $p$ -value are shown. RB1 mutated samples are labeled in dark orange.
- B) Frequency of the side chains observed in the detected lipids.
- C) Abundance of phosphatidylglycerol PG(18:2/22:6) across multi-omics subtypes and GTEx normal samples. 22:6 is likely DHA. Wilcoxon test  $p$ -value is labeled.
- D) Abundance of 22:6-carrying TGs across multi-omics subtypes and GTEx normal samples. 22:6 is likely DHA. Wilcoxon test  $p$ -value is labeled.
- E) Abundance of 22:6-carrying PC, PE and PS across multi-omics subtypes and GTEx normal samples. 22:6 is likely DHA. Wilcoxon test  $p$ -value is labeled.
- F) Scatterplot showing correlation between DHA abundance and PI(20:4/22:6) abundance. Pearson's correlation value and  $p$ -value are shown.
- G) PEs carrying 22:4 or 20:4 fatty acids are downregulated in nmf2/mesenchymal-like subtype, while PE not containing either of the two FAs is upregulated in IDH1 mutant subtype only.



Differential expression significance: Least significant (white) to Most significant (red). Missing protein expression data (grey box). Phosphosite (purple dot). Druggable gene (green box). Phosphorylation (blue arrow), Upregulates expression (green arrow).

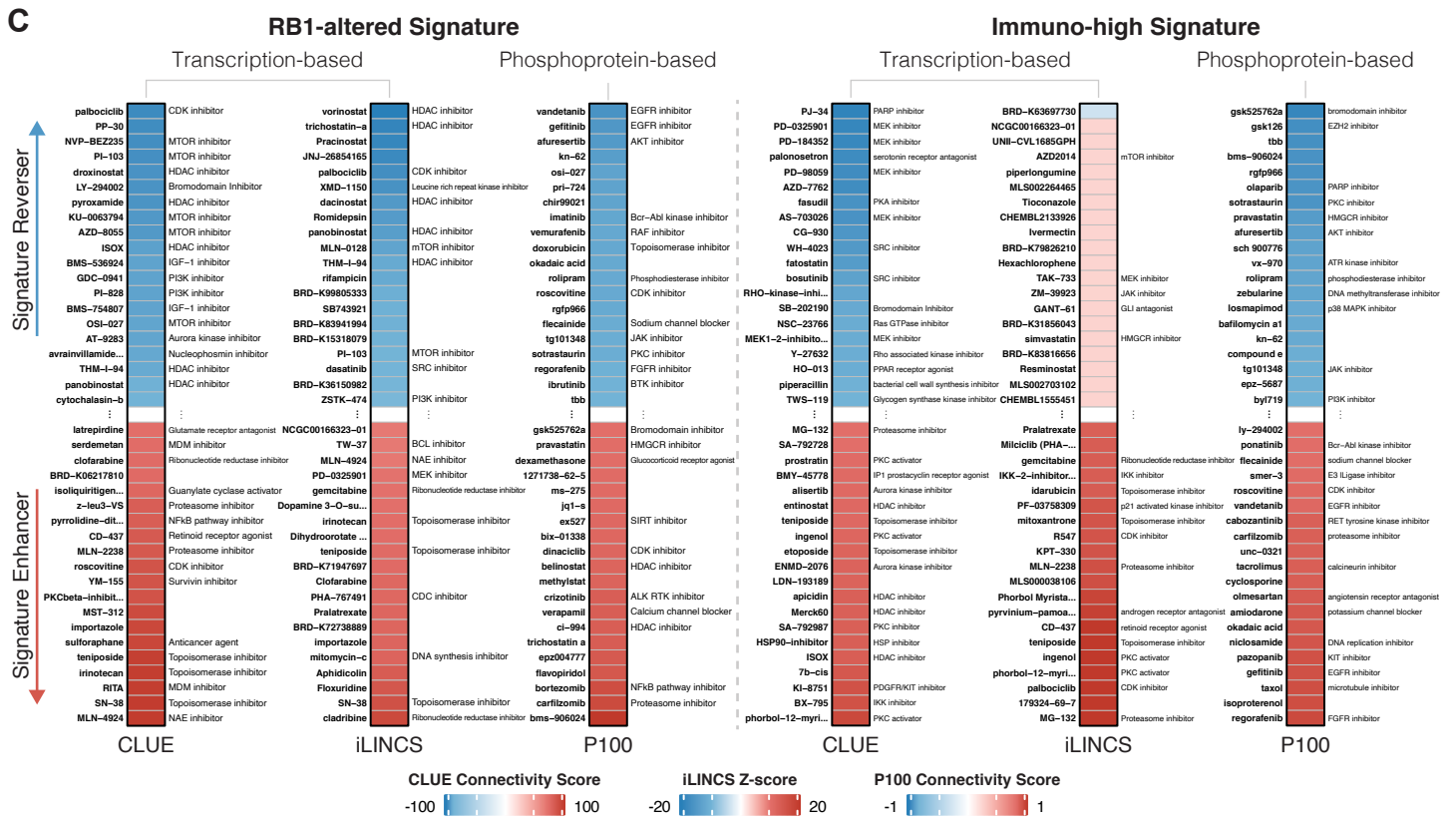
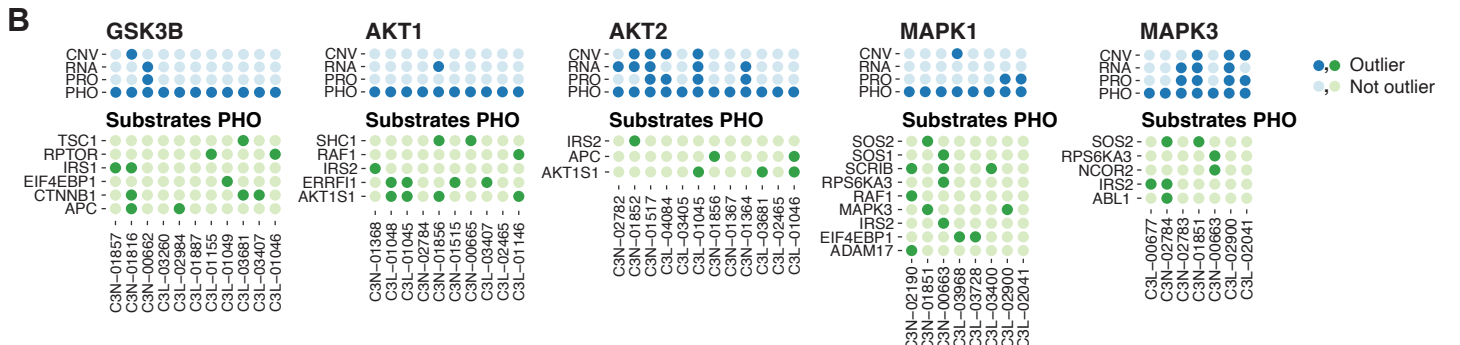




**Figure S7. Summary of Pathway Alterations of Mesenchymal Tumors Compared to the Other Tumors, Related to Figure 7.**

A) Causal explanations for differentially expressed proteomic and phosphoproteomic profiles in mesenchymal tumors versus the rest of the tumors using CausalPath. We highlighted the immune and hypoxia-related interactions enriched in the graph. Genes controlling the immune response might be a potential therapeutic target. Complete result graph is given in **Table S5**.

B) Sample level outlier status for kinase-substrate pairs shown in **Figure 7B**. For kinases (blue) outlier status for four levels of data is shown: CNV, RNA, PRO (protein) and PHO (phosphorylation). For their substrates (green) only PHO outlier status is shown.

C) Drug connectivity analysis using alteration-specific transcriptional (CLUE and iLINCS) and phosphoproteomic (P100) signatures of RB1 altered versus WT tumors and immune-high (im1, im2, and im3) versus immune-low (im4) tumors.